Reaction-diffusion patterning of DNA-based artificial cells

Adrian Leathers,[†] Michal Walczak,[†] Ryan A. Brady,[‡] Assala Al Samad,[¶,§] Jurij Kotar,[†] Michael J. Booth,[¶,§] Pietro Cicuta,[†] and Lorenzo Di Michele[*,‖,⊥,†]

†Biological and Soft Systems, Cavendish Laboratory, University of Cambridge, Cambridge CB3 0HE, UK

‡Department of Chemistry, Faculty of Natural and Mathematical Sciences, King's College London, London SE1 1DB, UK.

¶Chemistry Research Laboratory, University of Oxford, Oxford OX1 3TA, UK

§Department of Chemistry, University College London, London WC1H 0AJ, UK

‖Department of Chemistry, Imperial College London, Molecular Sciences Research Hub, London W12 0BZ, UK

⊥fabriCELL, Imperial College London, Molecular Sciences Research Hub, London W12 0BZ, UK

E-mail: l.di-michele@imperial.ac.uk

Abstract: Biological cells display complex internal architectures, with distinct micro environments that establish the chemical heterogeneity needed to sustain cellular functions. The continued efforts to create advanced cell mimics – *artificial cells* – demands strategies to robustly engineer micro-compartmentalised architectures, where the molecular makeup of distinct regions is coupled with localised functionalities. Here, we introduce a platform for constructing membrane-less artificial cells from the self-assembly of synthetic DNA nanostructures, in which internal domains can be established thanks to a rationally designed reaction-diffusion process. The method, rationalised through numerical modelling, enables the formation of up to five distinct and addressable environments, in which functional moieties can be localised. As a proof-of-concept, we apply this platform to build artificial cells in which a prototypical nucleus synthesises fluorescent RNA aptamers, which then accumulate in a surrounding storage shell, thus demonstrating spatial segregation of functionalities reminiscent of that observed in biological cells.

Bottom-up synthetic biology aims to engineer artificial systems that exhibit biomimetic structure and functionality from the rational combination of molecular and nanoscale elements. These systems often take the form of *artificial cells* (ACs), micro-robots constructed *de novo* to replicate behaviours typically associated with biological cellular life, including communication, adaptation, energy conversion, and motility.[1–3] If endowed with sufficiently advanced cell-like responses, ACs could underpin game-changing solutions in personalised diagnostics and therapeutics, green synthesis and environmental remediation.[1,4,5] Similar to their biological counterparts, ACs require a micro-compartmentalised architecture to regulate transport and establish internal heterogeneity, as typically necessary to sustain biomimetic molecular pathways.[6] AC compartments often

rely on lipid,[7,8] polymer[8,9] or protein membranes,[10] but membrane-less implementations based on coacervates[11–13] or hydrogels[14,15] are gaining traction, driven by enhanced robustness, easy manufacturing and the renewed interest for biomolecular condensates in cell biology.[16] While internal compartmentalisation can be robustly achieved in membrane-based platforms, *e.g.* through nesting or sequential assembly,[6] no general platform has been proposed to program local composition in membrane-less scaffolds. Here, we leverage the structural and dynamic programmability afforded by DNA nanotechnology[17,18] to construct membrane-less condensates of DNA nanostructures, which can be "patterned" thanks to a reaction-diffusion scheme.[19–22] This strategy can generate up to five chemically addressable, distinct micro-environments whose features can be rationalised through numerical modelling. As a proof-of-concept, we use the platform to create model ACs with compartmentalised functionality, namely where a fluorescent RNA aptamer is synthesised in a prototypical "nucleus" and accumulates in an outer shell.

Our condensates self-assemble from branched, amphiphilic DNA nanostructures, shown in Fig. 1A. Similar constructs were previously demonstrated to form nanoporous phases with programmable structure, molecular-sieving properties, stimuli responsiveness, and the ability to host dynamic DNA circuitry.[23–25,28,29] As depicted in Fig. 1B, Figure S1 (SI), and detailed in the Experimental Methods (SI), spherical aggregates with cell-like dimensions (10 - 40 μm in diameter) readily emerge from a one-pot annealing reaction. Small Angle X-Ray Scattering demonstrates that the condensates display internal crystalline order with a BCC unit cell and lattice parameter of 26.8 nm, consistently with previous observations on similar systems (Figure S2).[24]

The foundational building block used here consists of a DNA four-way junction, with cholesterol moieties labelling the end of each 35-base-pair (bp) duplex arm (Fig. 1A). One of the arms is modified with an additional single-stranded overhang to which a *base* (b) strand is connected. The base strand serves as a competitive binding site for freely diffusing *patterning strands* (p) of different lengths as depicted in Fig. 1A, where complementarity of domains is shown by same colouration and opposite directionality. All the patterning strands feature an identical (red) domain complementary to the base, but for longer strands complementarity is extended to more adjacent domains. This feature allows any longer patterning strand to displace a shorter strand from the base *via toehold mediated strand displacement* (toeholding),[26,27] but not *vice versa*, establishing a length-dependent binding hierarchy. The length of even the shortest binding domain (14 nucleotides - nt) is such that thermal detachment of the patterning strands does not occur within experimentally-relevant timescales. Sequences of all oligonucleotides are reported in Table S1, SI.

The principle for AC patterning is schematically depicted in Fig. 1C. Condensates are prepared hosting uniformly distributed base strands but without any patterning strands initially connected. Multiple types of patterning strands are then introduced in solution, with excess concentration compared to the number of available binding sites in the condensates (see Experimental Methods, SI). In this example, we introduce patterning strands p1 (16 nt) and p8 (40 nt) labelled with an Alexa 594 (red) and Alexa 488 (green), respectively. The diffusion coefficient of DNA increases with contour length,[30] and this dependency is enhanced in porous environments like our condensates,[31] allowing shorter DNA strands to diffuse significantly faster than longer ones. The shorter patterning strands, p1 in the example, will thus rapidly access the condensate occupying base strands progressively, from the outside of the condensate inwards. At later times, the longer p8 strand also diffuses through the condensate, and as it does it displaces p1 strands from the base *via* toeholding, releasing them back into solution. The result, experimentally demonstrated through confocal micrographs in
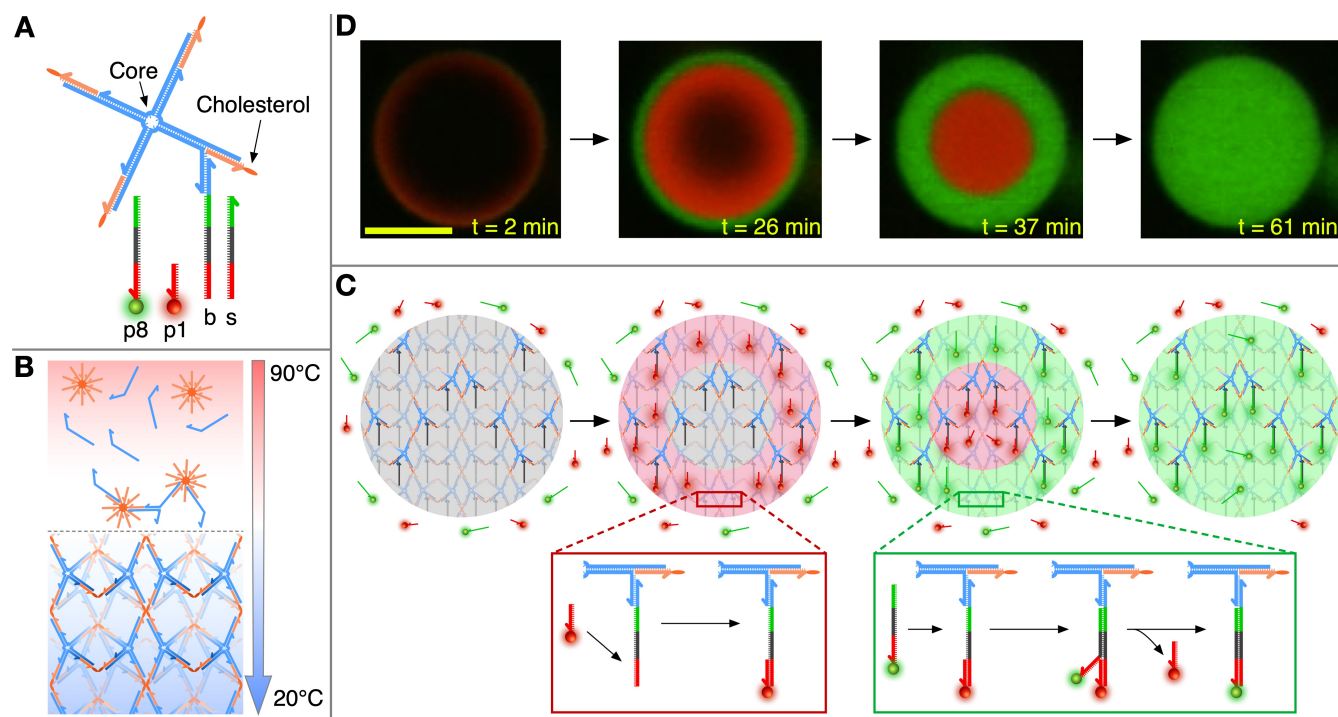
Figure 1: **Reaction-diffusion patterning of amphiphilic DNA condensates. A:** Foundational building block of the condensates consisting of a locked four-way DNA junction with cholesterol moieties at the end of each arm. The constructs are composed of four distinct strands forming the junction (blue) and four identical cholesterolised oligonucleotides (orange).[23–25] One arm features an additional overhang to which a *base* strand (b) is connected, which serves as a binding site for complementary, freely diffusing *patterning* strands. The latter range between 16 nt (p1) to 40 nt (p8) in length, and compete over (colour-coded) overlapping binding domains on the base strand. p1 and p8 shown here are functionalised with Alexa 594 (red) and Alexa 488 (green) fluorophores, respectively. The *stop* strand (s) has the same sequence as the base and can be added in solution to sequester the excess patterning strands. Sequences of all DNA oligonucleotides are provided in Table S1, SI. **B:** Assembly process for amphiphilic DNA condensates. Samples containing all single-stranded DNA components are slowly annealed from 90°C to 20°C leading to the formation of a nano-porous framework with the branched DNA motifs connecting micelle-like hydrophobic cores where the cholesterol modifications localise, as previously reported.[23–25] Details on sample preparation are provided in the Methods (SI). **C:** Schematic depiction of the designed reaction-diffusion pathway. At time $t = 0$, condensates are exposed to a solution of p1 (short, red) and p8 (long, green) patterning strands in excess concentration compared to base strands. Short p1 DNA strands are able to diffuse inside the condensates faster than long p8 strands, allowing for prior binding to the base strand (red box). At later times, p8 strands then diffuse within the condensates and, due to the sequence design, are able to displace p1 strands *via* toeholding[26,27] (green box). The result is a sequence of two fronts propagating inward through the condensate. **D:** Series of confocal micrographs of the process discussed in **C**, where propagating fronts are visualised thanks to fluorescent modifications of p1 and p8. Scale bar: 15 µm.

3

Fig. 1D, is a sequence of inward-propagating fluorescent fronts: a red wave corresponding to the rapidly diffusing p1 appears first, which is then replaced by a green front produced by the slowly diffusing but strongly binding p8 strands. Note that, in confocal measurements, signal from excess patterning strands in solution is not visible due to the comparatively much higher concentration of binding sites within the condensates.

This scheme thus allows us to localise different oligonucleotides in distinct and individually addressable concentric shells within the condensates. While in this example the patterning strands bear a simple fluorescent modification, one could easily envisage including functional elements, thus paving the way for compartmentalised functionality in membrane-less ACs, as discussed later.

Domain structure and evolution can be programmed *via* the number and length of patterning strands, as summarised in Fig. 2. Confocal micrographs for representative condensates exposed to one, two, three, and five patterning strands are shown in Fig. 2A-D while SI Videos S1-S12 exemplify pattern evolution in individual condensates and larger sample areas. On the right-hand-side of Fig. 2, colour maps represent the time evolution of the radially-averaged fluorescent intensity (see Experimental Methods). Examples of analogous colour maps for multiple condensates and different numbers of patterning strands are shown in Figs S3-6. For tests with more that two domains, non-fluorescent (dark) patterning strands of lengths intermediate between two fluorescent ones were used. For instance, in Fig. 2C, a dark 30 nt strand (p6) is used in combination with 16 nt (red) p1 and 40 nt (green) p8, generating a dark shell that separates the fast-propagating red wave and the slowest-propagating green wave. Two dark (p3, p7) and three fluorescent strands (p1, p5, p8) are used in Fig. 2D, generating five distinct micro-environments at ~ 7 minutes from the exposure to the patterning strands, as highlighted by the radially averaged fluorescent-intensity profiles (right). Note that

in this case the difference in length between adjacent species varies between 5 and 7 nt, demonstrating a separation ability comparable with electrophoretic techniques and hinting at possible applications of the ACs for the detection and separation of nucleic acids. For a fixed number of patterning strands, the relative width of the domains can be controlled by design, as shown in Fig. S7 for three-domain experiments where dark strands of different lengths are used.

In all examples discussed, the reactions are designed to progress towards the equilibrium configuration in which the longest, most stable construct occupies all binding sites, defying the purpose of our solution as a means of engineering AC compartmentalisation. Pattern evolution can however be readily arrested using a *stop* strand (s, Fig. 1A), with sequence identical to that of the base. The stop strand is added in solution with excess concentration compared to that of all patterning strands combined (see Experimental Methods), sequestering them and interrupting wavefront propagation. Figure 2E shows that patterns arrested with this protocol remain stable for several hours, as required for the purpose of compartment engineering in ACs.

The system's evolution can be modelled through a set of coupled reaction-diffusion equations under the assumption of a spherical condensate geometry and excess patterning strands in solution, as fully detailed in the Modelling Methods (SI). Alongside known or easily determined system parameters such as condensate size, the model requires as input the diffusion constants (D) of the patterning strands, the second-order rate constants through which the patterning strands bind the base and/or displace previously bound strands (k_{on}), and the exchange rate of patterning strands between the bulk and the condensate (k_{in}).[32,33] The latter three quantities (D, k_{on} and k_{in}) are used as fitting parameters. The model also features a partition coefficient of the patterning strands within the condensates[32] that, for realistic values, is found to

4
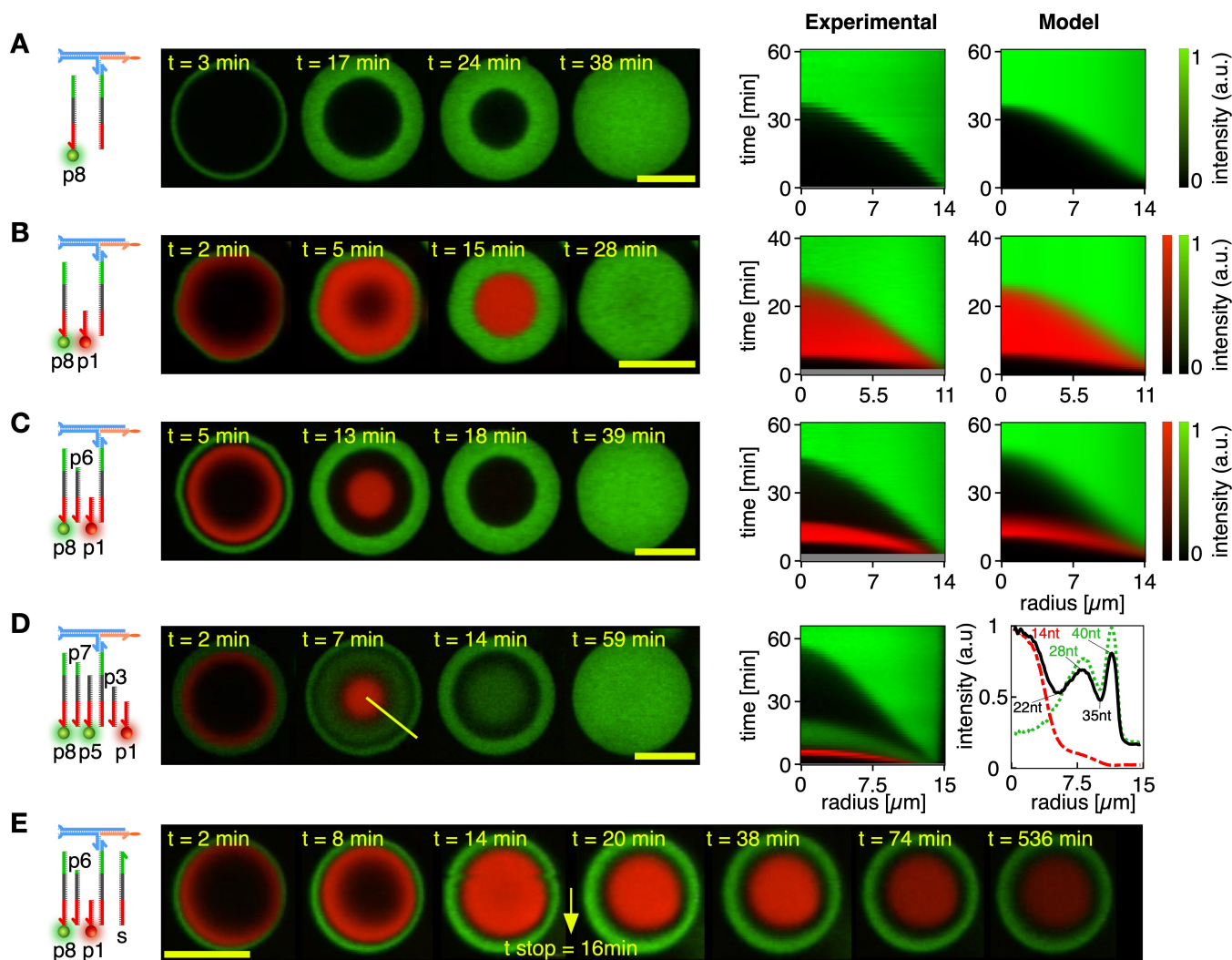
Figure 2: **Condensate patterning is predictable and customisable. A-D:** Patterning-strand scheme (left) and confocal microscopy data (centre) for condensates patterned to form an increasing number of concentric domains, from one in **A** to five in **D**. Some patterning strands are fluorescently labelled with Alexa 594 (p1) and Alexa 488 (p5, p8), while others do not bear modifications, hence resulting in dark regions intermitting fluorescent shells in confocal data. See Table S1 (SI) for DNA sequences. The time evolution of the domain structure is visualised by plotting the averaged radial fluorescence profile, which for systems **A-C** is compared with the fitted outcome of a reaction-diffusion numerical model (right). Note that early times are not shown in experimental colour maps (gray bands) due to a delay between the time at which condensates are exposed to patterning strand ($t = 0$) and the start of confocal recording. See Methods (SI) for information on image analysis and numerical modelling. For system **D**, on the right we show a radial intensity profile computed from confocal images at $t = 7$ min, highlighting the presence of five distinct domains. The green dotted and red dashed lines mark the signal from the Alexa 488 (p5, p8) and Alexa 594 (p1) channels, respectively, while the black solid line represents the overall intensity. All profiles are normalised by their highest value. **E:** Domain propagation can be arrested by adding an excess of the stop strand (s) in solution (see Fig. 1A), here demonstrated with confocal data for a system with three patterning strands (p1, p6, p8). The stop strand is added at $t = 16$ min, after which no further pattern evolution is observed (besides photobleaching). Videos S1-S8 show pattern evolution in individual condensates (even numbered) and larger fields of view (odd numbered). Scale bars: 15 µm.

5

A

B
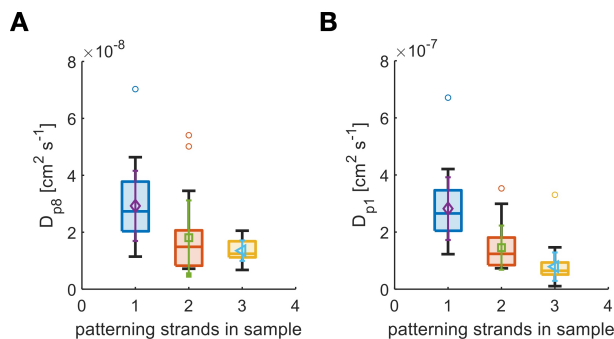
Figure 3: **Model fitting enables extraction of diffusion constant** Diffusion coefficients for 40 nt patterning strand p8 (**A**) and 16 nt patterning strand p1 (**B**). Data are shown for samples with one patterning strand (p1 or p8; Fig. 2A and Figs S3-4; $N = 33$ condensates for p1 and $N = 29$ condensates for p8), two patterning strands (p1 and p8; Fig. 2B and Fig. S5; $N = 23$ condensates) and three patterning strands (p1, p6, and p8; Fig. 2C and Fig. S6; $N = 43$ condensates). The results are displayed as box plots with highlighted median, upper and lower quartiles (box), and 50th and 50th centiles (whiskers) outliers excluded. Overlaid to the box plots are the mean (symbol) and standard deviation (same-colour errorbar) of the distributions.

have no significant effect on the fitting outcomes, and was thus set to 1 (Fig. S8).

Numerical solutions of the model are fitted to confocal data, accounting for diffraction-induced blurring (see Modelling Methods), for up to three competing patterning strands. Comparison between experimental reaction-diffusion maps and the fitted model outcomes demonstrates near-quantitative agreement, as shown in Fig. 2 (right) and Figs S3-6. Small differences may emerge due to early-time effects related to sample mixing, optical artefacts due to refractive-index mismatches and absorption, non-spherical condensate geometry, or non-isotropic diffusion caused by the contact with the bottom of the experimental chamber.

Figure 3 summarises the distributions of fitted diffusion constants for our shortest (p1, 16 nt) and longest (p8, 40 nt) patterning

strands, as determined for experiments with a single patterning strand (p1 or p8; Fig. 2A and Figs S3-4), two patterning strands (p1 and p8; Fig. 2B and Fig. S5), and three patterning strands (p1, p6, and p8; Fig. 2C and Fig. S6).

We observe an order-of-magnitude difference in diffusion constant between p1 and p8, with $D_{p1} = 1-4\times10^{-7}$ cm^2 s^{-1} and $D_{p8} = 1-4\times10^{-8}$ cm^2 s^{-1}. D is the primary parameter that determines the propagation speed of the reaction-diffusion fronts through the condensates, therefore, the difference found between D_{p1} and D_{p8} is consistent with expectations. We further note that both diffusion constants decrease in the presence of additional patterning strands, hinting at crowding effects.

Figure S9A shows the fitting outcomes for rate constant k_{on}. In all cases, $k_{on, p1}$ describes binding of p1 to a free base strand, given that p1 is unable to displace other incumbent strands. Similarly, $k_{on, p8}$ describes hybridisation to free base strands in experiments only featuring p8. When shorter patterning strands are present alongside p8, $k_{on, p8}$ can be interpreted as the effective second-order rate constant of the toehold-mediated strand displacement reaction through which p8 displaces incumbent p1 (2-strand case) and p6 (3-strand case).[26] Fits produce values of $k_{on, p1}$ and $k_{on, p8}$ within the same order of magnitude ($10^4 - 10^5$ M^{-1} s^{-1}), with the former slightly larger than the latter. Values are consistent with previous observations for hybridisation in hydrogels,[20] and smaller than rates typically measured in freely diffusing constructs ($\sim 10^6$ M^{-1} s^{-1}).[26] The similarity between rates of hybridisation ($k_{on, p1}$) and toeholding ($k_{on, p8}$) is expected, given that the two are known to converge for toehold lengths in excess of 6 nt – a condition that is verified in our reactions.[26] A decreasing trend is found with increasing number of patterning strands, which is much more pronounced for $k_{on, p8}$ compared to $k_{on, p1}$ and may thus be due to crowding.

We note that while D is the primary regulator of the wavefront propagation speed, k_{on} influ-

ences the width (or sharpness) of the front, with large rates producing sharper profiles. In experiments, however, the fluorescent features are also blurred by diffraction. We observe that the diffraction-induced blurring of the wavefronts dominates over that associated to changes in k_{on} when the latter drops below $\sim 10^5 \, \mathrm{M}^{-1} \, s^{-1}$, indicating that the model becomes insensitive to changes in the binding/toeholding constants when these take higher values. The fitting outcomes in Figure S9A are close to the limit of sensitivity of the model, and thus their quantitative interpretation should be done with caution (see Modelling Methods for details).

The material exchange rate k_{in}, as summarised in Fig. S9B, is slightly larger for p1, compared with p8, consistent with the higher diffusion rate of the shorter patterning strand, while no clear trend is observed as a function of the number of patterning strands.

Having identified a route for establishing addressable domains in condensates, we can proceed with localising functional elements within different compartments to create a model membrane-less AC hosting a spatially organised pathway. As summarised in Fig 4A, the AC has been patterned with a "nucleus" region hosting a *template* construct (t), containing a T7 promoter sequence and the DNA complementary sequence to an RNA aptamer, and the shell region containing binding sites for the RNA product. The template is anchored to the base strand through a *bridging* (r) strand, which ensures the formation of the double-stranded T7 promoter required for the T7 polymerase to begin transcription.[34] The RNA produced is a modified version of the DFHBI-binding fluorescent Broccoli aptamer.[35] Addition of an extra 8 bps to the stem region produced a significantly brigher aptamer as discussed in the Experimental Methods and Fig. S10. The aptamer also features a binding site complementary to the single-stranded overhang present in the *capture* (c) strands located in the shell region. See Experimental Methods for full details on the patterning process.

The sought response at the AC level is sketched in Fig. 4B. Patterned ACs are exposed to polymerase that, similar to other proteins of comparable size,[24] can diffuse through the condensates, reaching the template in the nucleus. Here, the Broccoli aptamer is produced, which readily binds to DFHBI and diffuses out towards the shell and binds the capture motifs.

Figure 4C (top) shows a time-resolved sequence of confocal micrographs from an AC producing the designed response. The nucleus (cyan), fluorecently stained thanks to a fluorophore on the bridging strand, retains the same size through the experiment and only undergoes progressive bleaching. In turn, fluorescence from the Broccoli aptamer (orange) builds up in the shell region from the inside-out, consistent with the RNA product being produced in the nucleus. Combined bright field / confocal micrographs of the same objects confirm that the overall size and appearance of the condensate does not change during Broccoli build up (Fig. 4C, bottom). In Fig. 4D we show a colour map of the radial intensity of the Broccoli emission versus time, where the outwards-propagating front is clearly observable, marked by an arrow. Data from more ACs with different shell thicknesses relative to nucleus size are summarised in Fig. S11, while time lapses of the process can be inspected in SI Videos S13-S16. As a control, in Fig. S12 we show the results of experiments with template/promoter constructs free in solution, which expectedly show outside-in accumulation. Finally, in Figs S13 and S14 we report the time-dependent Broccoli emission in bulk fluorimetry experiments, including samples with aptamer-expressing ACs and samples that only contain the supernatant solution but no ACs. The lack of signal from the latter further confirms that aptamer production occurs exclusively within the AC nucleus.

In summary, we have introduced a general process for the creation of stable and individually addressable domains in condensates self-assembled from DNA nanostructures. The process relies on a reaction-diffusion scheme, where
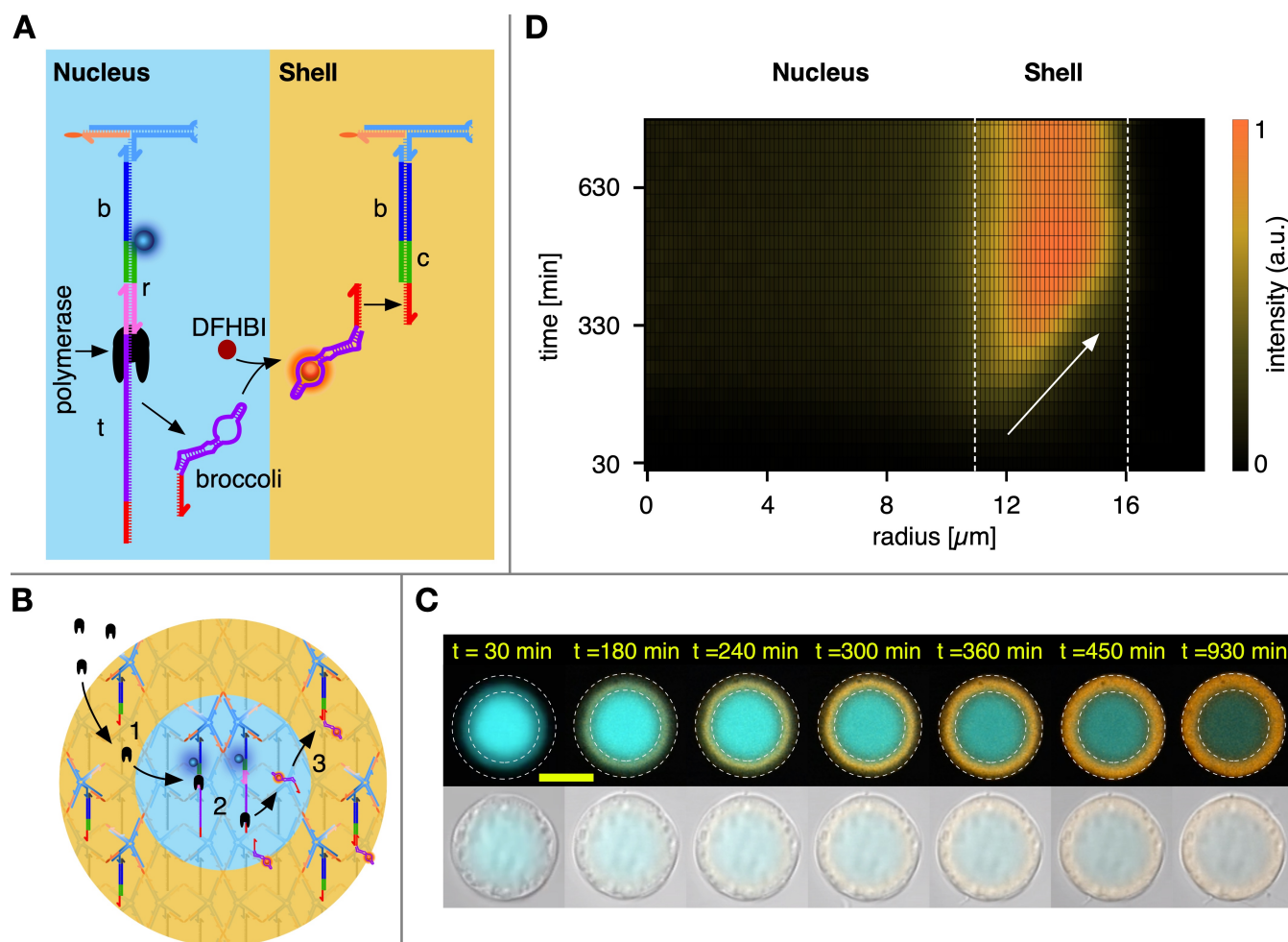
Figure 4: **Compartmentalised functionality in a model artificial cell. A:** Schematics of the functional nucleic acid machinery in *nucleus* (cyan) and *shell* regions (orange). In the nucleus, connected to the base strand are a *bridge* (r) strand and the *template* (t) strand. Together, these form a double stranded T7 promoter (pink) and a single stranded polymerase template (purple, red) from which a polymerase (black) is able to synthesise Broccoli RNA aptamers (folded purple and red) that form a complex with DFHBI molecules to become fluorescent (orange). The base strands in the shell region are connected to *capture* strands (c) with single stranded overhangs (red) complementary to a free domain on the broccoli aptamer. Complementary DNA/RNA domains are shown in the same colour. Protocols for patterning the ACs are detailed in the Experimental Methods (SI). **B:** Mode of operation of the AC. The polymerase is added in solution alongside NTPs, DFHBI, and other components required for Broccoli synthesis, which diffuse through the shell (1) reaching the nucleus, where the aptamers are produced (2). The aptamers then diffuse outwards and bind to the dedicated sites in the shell (3). **C:** A series of confocal images (top) of an AC progressively building up Broccoli aptamer in the shell (orange). Note how the signal accumulates from the nucleus-shell interface and propagates outwards. The nucleus is shown in cyan, and progressively photobleaches. The dashed lines mark the physical boundary of the AC and that between the nucleus and the shell. Bottom: bright field images of the same AC overlaid to (faint) confocal data, demonstrating that no physical change to the AC occurs during Broccoli synthesis. The reaction is initiated at time $t = 0$, as discussed in the Experimental Methods (SI). **D:** colour map showing the evolution of the radial fluorescent intensity of the aptamer. The slope of the fluorescent front signals accumulation from the inside-out, as highlighted by the white arrow. Dashed lines mark the nucleus/shell and shell/solution boundaries. Videos S13-S16 show the response of multiple ACs with different shell/nucleus size ratios. Scale bar: 15 μm.

patterning constructs with different diffusivities and binding affinities compete for binding sites within the condensates. The number and size of the domains can be tuned by design and predicted by numerical modelling. As a proof-of-concept, we apply the patterning scheme to construct a model artificial cell with an active nucleus that produces a fluorescent RNA aptamer, and a storage shell where the product progressively accumulates. We argue that reaction-diffusion patterned DNA condensates could constitute a versatile platform for engineering cell-like agents with spatially-resolved functionality. Potential responses are not limited to expression or capture of RNA products, as the domains can be enriched with virtually any functional molecule or nanoscale agent that can be linked to the patterning strands, including enzymes, nanoparticles, aptamers and photo-responsive elements, thus unlocking the opportunity to engineer ever more complex reaction pathways within the ACs. Finally, while here DNA condensates are used as passive scaffolds, one can envisage design modifications where patterning dynamically alters the local physical structure by modifying mesh size and rheological properties. These solutions, could enable the design of feedback systems where local transport properties change in response to AC activity, bringing us closer to synthetically replicating the structure-function synergy that characterises biological cells.

References

(1) Buddingh', B. C.; van Hest, J. C. M. Artificial Cells: Synthetic Compartments with Life-like Functionality and Adaptivity. *Acc. Chem. Res.* **2017**, *50*, 769–777.

(2) Lentini, R.; Yeh Martín, N.; Mansy, S. S. Communicating artificial cells. *Curr. Opin. Chem. Biol.* **2016**, *34*, 53–61.

(3) Stano, P. Is Research on "Synthetic Cells" Moving to the Next Level? *Life* **2019**, *9*.

(4) van Stevendaal, M. H. M. E.; van Hest, J. C. M.; Mason, A. F. Functional Interactions Between Bottom-Up Synthetic Cells and Living Matter for Biomedical Applications. *ChemSystemsChem* **2021**, *3*, e210000.

(5) Smith, J. M.; Chowdhry, R.; Booth, M. J. Controlling Synthetic Cell-Cell Communication. *Front. Mol. Biosci* **2022**, *8*, 809945.

(6) Trantidou, T.; Friddin, M.; Elani, Y.; Brooks, N. J.; Law, R. V.; Seddon, J. M.; Ces, O. Engineering Compartmentalized Biomimetic Micro- and Nanocontainers. *ACS Nano* **2017**, *11*, 6549–6565.

(7) Elani, Y.; Gee, A.; Law, R. V.; Ces, O. Engineering multi-compartment vesicle networks. *Chem. Sci.* **2013**, *4*, 3332–3338.

(8) Rideau, E.; Dimova, R.; Schwille, P.; Wurm, F. R.; Landfester, K. Liposomes and polymersomes: a comparative review

towards cell mimicking. *Chem. Soc. Rev.* **2018**, *47*, 8572–8610.

(9) LoPresti, C.; Lomas, H.; Massignani, M.; Smart, T.; Battaglia, G. Polymersomes: nature inspired nanometer sized compartments. *J. Mater. Chem.* **2009**, *19*, 3576–3590.

(10) Joesaar, A.; Yang, S.; Bögels, B.; van der Linden, A.; Pieters, P.; Kumar, B. V. V. S. P.; Dalchau, N.; Phillips, A.; Mann, S.; de Greef, T. F. A. DNA-based communication in populations of synthetic protocells. *Nat. Nanotechnol.* **2019**, *14*, 369–378.

(11) Altenburg, W. J.; Yewdall, N. A.; Vervoort, D. F.; van Stevendaal, M. H.; Mason, A. F.; van Hest, J. C. Programmed spatial organization of biomacromolecules into discrete, coacervate-based protocells. *Nat. Commun.* **2020**, *11*, 1–10.

(12) Simon, J. R.; Carroll, N. J.; Rubinstein, M.; Chilkoti, A.; López, G. P. Programming molecular self-assembly of intrinsically disordered proteins containing sequences of low complexity. *Nat. Chem.* **2017**, *9*, 509–515.

(13) Qiao, Y.; Li, M.; Booth, R.; Mann, S. Predatory behaviour in synthetic protocell communities. *Nat. Chem.* **2017**, *9*, 110–119.

(14) Sato, Y.; Sakamoto, T.; Takinoue, M. Sequence-based engineering of dynamic functions of micrometer-sized DNA droplets. *Science Advances* **2020**, *6*, eaba3471.

(15) Aufinger, L.; Simmel, F. C. Artificial Gel-Based Organelles for Spatial Organization of Cell-Free Gene Expression Reactions. *Angew. Chem. Int. Ed.* **2018**, *57*, 17245–17248.

(16) Sehgal, P. B.; Westley, J.; Lerea, K. M.; DiSenso-Browne, S.; Etlinger, J. D. Biomolecular condensates in cell biology and virology: Phase-separated membraneless organelles (MLOs): Biomolecular condensates in cell biology and virology. *Anal. Biochem.* **2020**, *597*, 113691.

(17) Seeman, N. C.; Sleiman, H. F. DNA nanotechnology. *Nat. Rev. Mater.* **2017**, *3*, 17068.

(18) Rubio-Sánchez, R.; Fabrini, G.; Cicuta, P.; Di Michele, L. Amphiphilic DNA Nanostructures for Bottom-Up Synthetic Biology. *Chem. Commun.* **2021**, –.

(19) Abe, K.; Kawamata, I.; Nomura, S. I. M.; Murata, S. Programmable reactions and diffusion using DNA for pattern formation in hydrogel medium. *Mol. Syst. Des. Eng.* **2019**, *4*, 639–643.

(20) Chen, S.; Seelig, G. Programmable patterns in a DNA-based reaction-diffusion system. *Soft Matter* **2020**, *16*, 3555–3563.

(21) Zadorin, A. S.; Rondelez, Y.; Gines, G.; Dilhas, V.; Urtel, G.; Zambrano, A.; Galas, J. C.; Estevez-Torres, A. Synthesis and materialization of a reaction-diffusion French flag pattern. *Nat. Chem.* **2017**, *9*, 990–996.

(22) Scalise, D.; Schulman, R. Designing modular reaction-diffusion programs for complex pattern formation. *Technology* **2014**, *02*, 55–66.

(23) Brady, R. A.; Brooks, N. J.; Cicuta, P.; Michele, L. D. Crystallization of Amphiphilic DNA C-Stars. *Nano Lett.* **2017**, *17*, 3276–3281.

(24) Brady, R. A.; Brooks, N. J.; Foderà, V.; Cicuta, P.; Michele, L. D. Amphiphilic-DNA Platform for the Design of Crystalline Frameworks with Programmable Structure and Functionality. *J. Am. Chem. Soc.* **2018**, *140*, 15384–15392.

(25) Brady, R. A.; Kaufhold, W. T.; Brooks, N. J.; Foderà, V.; Di Michele, L. Flexibility defines structure in crystals of amphiphilic DNA nanostars. *J. Phys. Condens. Matter* **2019**, *31*, 074003.

(26) Zhang, D. Y.; Winfree, E. Control of DNA strand displacement kinetics using toehold exchange. *J. Am. Chem. Soc.* **2009**, *131*, 17303–17314.

(27) Simmel, F. C.; Yurke, B.; Singh, H. R. Principles and Applications of Nucleic Acid Strand Displacement Reactions. *Chem. Rev.* **2019**, *119*, 6326–6369.

(28) Fabrini, G.; Minard, A.; Brady, R. A.; Di Antonio, M.; Di Michele, L. Cation-Responsive and Photocleavable Hydrogels from Noncanonical Amphiphilic DNA Nanostructures. *Nano Lett.* **2022**, *22*, 602–611.

(29) Walczak, M.; Brady, R. A.; Mancini, L.; Contini, C.; Rubio-Sánchez, R.; Kaufhold, W. T.; Cicuta, P.; Di Michele, L. Responsive core-shell DNA particles trigger lipid-membrane disruption and bacteria entrapment. *Nat. Commun.* **2021**, *12*, 4743.

(30) Stellwagen, E.; Lu, Y.; Stellwagen, N. C. Unified description of electrophoresis and diffusion for DNA and other polyions. *Biochemistry* **2003**, *42*, 11745–50.

(31) Pluen, A.; Netti, P. A.; Jain, R. K.; Berk, D. A. Diffusion of macromolecules in agarose gels: Comparison of linear and globular configurations. *Biophys. J.* **1999**, *77*, 542–552.

(32) Schuck, P. Kinetics of ligand binding to receptor immobilized in a polymer matrix, as detected with an evanescent wave biosensor. I. A computer simulation of the influence of mass transport. *Biophys. J.* **1996**, *70*, 1230–1249.

(33) Crank, J. The mathematics of diffusion. 2nd Edn. **1979**,

(34) Kar, S.; Ellington, A. D. Construction of synthetic T7 RNA polymerase expression systems. *Methods* **2018**, *143*, 110–120.

(35) Filonov, G. S.; Moon, J. D.; Svensen, N.; Jaffrey, S. R. Broccoli: Rapid Selection of an RNA Mimic of Green Fluorescent Protein by Fluorescence-Based Selection and Directed Evolution. *J. Am. Chem. Soc.* **2014**, *136*, 16299–16308.